

Article

Assembly Strategy for Modular Components Using a Dual-Arm Space Robot with Flexible Appendages

Shuji Yang, Yonglei Zhang, Ti Chen , Hao Wen * and Dongping Jin

State Key Laboratory of Mechanics and Control of Mechanical Structures, Nanjing University of Aeronautics and Astronautics, 29 Yudao Street, Nanjing 210016, China

* Correspondence: wenhao@nuaa.edu.cn; Tel.: +86-025-8489-1672

Abstract: Space robotic systems tend to be more flexible and equipped with some appendages, such as solar panels and communication antennas. The inevitable vibration in the flexible appendage will occur during space missions, and it in turn affects the attitude of the rigid base due to coupling dynamics. This study develops an assembly scheme for a dual-arm space robot with flexible appendages to assemble two modular components and to minimize the disturbance force caused by the manipulators to the base and flexible appendages. The assembly strategy consists of two stages, a preassembly stage which transports the two components to desired relative states, and a trajectory tracking stage to achieve the final assembly. In the first stage, based on a relative Jacobian matrix in the base frame, an optimal objective function is formulated in terms of the relative position and attitude errors between the two components. Thereby, more freedom of manipulators is released for minimizing disturbance forces. Notably, two virtual points are created to describe the relative position between the two components. In the second stage, two components are driven to follow a relative trajectory for the final assembly with an unchanged relative attitude. Finally, numerical simulations are conducted to demonstrate the efficiency of the proposed assembly strategy.

Keywords: space robot; flexible appendages; assembly; two stages



Citation: Yang, S.; Zhang, Y.; Chen, T.; Wen, H.; Jin, D. Assembly Strategy for Modular Components Using a Dual-Arm Space Robot with Flexible Appendages. *Aerospace* **2022**, *9*, 819. <https://doi.org/10.3390/aerospace9120819>

Academic Editor: Gokhan Inalhan

Received: 28 October 2022

Accepted: 12 December 2022

Published: 13 December 2022

Publisher's Note: MDPI stays neutral with regard to jurisdictional claims in published maps and institutional affiliations.



Copyright: © 2022 by the authors. Licensee MDPI, Basel, Switzerland. This article is an open access article distributed under the terms and conditions of the Creative Commons Attribution (CC BY) license (<https://creativecommons.org/licenses/by/4.0/>).

1. Introduction

With the development of space technology, the number of space activities in various forms has increased in recent years [1–6]. For future space explorations, ultra-large space structures such as astronomical telescopes, solar power stations, and large hoop antennas are in great demand [7,8]. In view of their enormous sizes and launch abilities, the current deployable strategy that makes structures unfolded after reaching the orbit is not applicable [9]. As an appealing solution, the on-orbit assembly technique with the help of space robots is expected to construct the extremely large space structure, where small modular components are separately launched to the space and assembled on-orbit in a stage-by-stage manner. The assembly form generally contains two types. One is that a modular part is mounted on a spacecraft and assembled via rendezvous and docking [7,10,11]. The other utilizes a specific space robot with manipulators to achieve assembly of modular components [12,13]. The latter type is of particular interest in this work.

Several types of space robots, primarily walking robots on large space structures and free-flying robots with independent thrusters, have been studied to construct the large space structure. Staritz et al., reported on the first-generation walking robot Skyworker, comprising mechanical grippers to walk on large-scale orbital facilities and manipulators to perform inspection, maintenance, and assembly missions [14]. Hu et al., developed a formation control scheme of walking robots to construct a large solar sail using a sliding mode controller [15]. Recently, Cao et al., proposed an assembly strategy for a space robot attached to an orb-shaped solar array, wherein the motion planning of the robot for assembly is based on a vehicle–bridge coupled dynamic model [12]. However, walking

robots cannot perform well in the complex practical assembly process, e.g., constructing modular mirror components. In comparison, a free-flying robot is more versatile and accessible to manipulate [16–18]. Over past decades, considerable efforts containing numerical simulations and ground experiments have been made in space assembly works using this type of robot. Senda et al., conducted a truss assembly strategy based on a reinforcement learning strategy and performed the experiment using a space robot simulator including two manipulators and a satellite vehicle [19]. Boning et al., developed a control scheme for a team of free-flying robots to construct larger flexible structures, and it was validated by an air-bearing-based space robot simulator equipped with force and torque sensors [20]. Recently, Karumanchi et al., have proposed a payload-centric autonomy paradigm for assembling space modular structures, and it was achieved using a dual-arm robot called RoboSimian [21]. Lu et al., have designed a learning controller and some cooperative modular components for simulating the autonomous space assembly using a ground-fixed manipulator [22].

It is noted that most space robots in the abovementioned studies were assumed to be rigid, multibody systems. Actually, flexible appendages are mounted on the space robot, such as solar panels and communication antennas. Moreover, when manipulators move for assembly, it will cause the vibration of flexible appendages and changes in base attitudes, which may lead to loss of communication with the data relay satellite or the ground station. Hence, some efforts have been devoted to the research about space robots with flexible appendages in recent years. Yu et al., developed a dynamic model for a 6-DOF space robot with flexible panels using the single-direction recursive construction method and the Jourdain velocity variation principle [23]. Gasbarri and Pisculli proposed two new control strategies for robotic arms mounted on a flexible orbiting platform to compensate the flexibility excitations induced by the chaser satellite solar panels based on a mixed NE/EL dynamics formulation [24]. Xu et al., presented a recursive dynamic model and path planning scheme for a spacecraft mounted with manipulators and flexible appendages to capture a large flexible spacecraft [25]. Meng et al., introduced a dynamic model for a space robot with a flexible solar paddle treated as a lumped mass with the stiffness and employed a hybrid controller based on wave-based and PD control to remove the vibration when berthing the target [26]. Afterwards, in order to achieve a capture task, Meng et al., implemented an energy-based joint controller for time-varying trajectories due to flexible appendages and demonstrated it using a single-degree-of-freedom space robot experimental system [27].

It is worth noting that most of the current assembly strategies using free-flying robots focused on assembling small components individually to a large base structure, which was usually assumed to be resident to simplify the analysis. As shown in Figure 1, it is a feasible solution to improve assembly efficiency through constructing a large space structure in a level-by-level manner: assemble the smallest modular components into a sub-structure, and then assemble the sub-structure into a larger sub-structure or a base structure [13]. Hence, a two-stage assembly strategy for assembling two modular components using a free-flying dual-arm space robot with flexible appendages is studied in this work. The scheme is divided into preassembly and trajectory tracking stages at a dynamics level, where the flexible appendages are considered as two beam elements through a finite element means. In the preassembly stage, two components are driven to attain a predefined relative position and attitude, employing a relative Jacobian matrix in the base frame rather than the generalized one in the inertial frame. Besides, the disturbance force caused by movements of the manipulators is incorporated into the objective function. In the trajectory tracking stage, two components are planned to follow a relative trajectory for assembling while the relative attitude between them is kept unchanged. Finally, the presented two-stage assembly scheme is validated through numerical simulations.



Figure 1. Assembling modular components using a dual-arm space robot with flexible appendages.

The remainder of this paper is organized as follows. In Section 2, the dynamic model of a dual-arm space robot with flexible appendages is established. Afterwards, a two-stage control scheme is introduced to achieve assembly and optimization for the response of the base and flexible appendages in Section 3. Thereafter, in Section 4, numerical simulations are carried out for a dual-arm space robot with two three-DOF arms to verify the presented strategy, followed by the conclusions in Section 5.

2. Dynamics of a Dual-Arm Space Robot with Flexible Appendages

As shown in Figure 2, the planar dual-arm space robot system of concern consists of a base, two flexible appendages, and arms with revolute joints. The two arms and appendages are marked by numbers 1 and 2 on the left and right sides, respectively. The symbols Σ_I and Σ_B denote the inertial and the base frame, respectively. The orange and red lines represent the local frames of the two appendages. r_0 denotes a location vector of the base mass center, $\theta = [\theta_1^{(1)} \ \dots \ \theta_{n_2}^{(2)}]^T$ and θ_0 are rotation angles of the base and manipulators, respectively, and $r_i^{(1)}$ and $r_j^{(2)}$ represent mass center vectors of link i in arm 1 and link j in arm 2. For the planar case discussed in this paper, one obtains:

$${}^{(I)}r_i^{(1)} = {}^{(I)}r_{i-1}^{(1)} + \frac{l_{i-1}^{(1)}}{2} \begin{bmatrix} \cos(\theta_{i1}^{(1)}) \\ \sin(\theta_{i1}^{(1)}) \end{bmatrix} + \frac{l_i^{(1)}}{2} \begin{bmatrix} \cos(\theta_{i1}^{(1)} + \theta_i^{(1)}) \\ \sin(\theta_{i1}^{(1)} + \theta_i^{(1)}) \end{bmatrix} \quad (i > 1) \quad (1)$$

$$\theta_{i1}^{(1)} = \theta_0 + \sum_{k1=1}^{i-1} \theta_{k1}^{(1)} \quad (2)$$

$${}^{(I)}r_1^{(1)} = {}^{(I)}r_0 + \sqrt{2}l_0 \begin{bmatrix} \cos(\frac{3\pi}{4} + \theta_0) \\ \sin(\frac{3\pi}{4} + \theta_0) \end{bmatrix} + \frac{l_1^{(1)}}{2} \begin{bmatrix} \cos(\theta_1^{(1)} + \theta_0) \\ \sin(\theta_1^{(1)} + \theta_0) \end{bmatrix} \quad (3)$$

$${}^{(I)}r_j^{(2)} = {}^{(I)}r_{j-1}^{(2)} + \frac{l_{j-1}^{(2)}}{2} \begin{bmatrix} \cos(\theta_{j2}^{(2)}) \\ \sin(\theta_{j2}^{(2)}) \end{bmatrix} + \frac{l_j^{(2)}}{2} \begin{bmatrix} \cos(\theta_{j2}^{(2)} + \theta_j^{(2)}) \\ \sin(\theta_{j2}^{(2)} + \theta_j^{(2)}) \end{bmatrix} \quad (j > 1) \quad (4)$$

$$\theta_{j2}^{(2)} = \theta_0 + \sum_{k2=1}^{j-1} \theta_{k2}^{(2)} \quad (5)$$

$${}^{(I)}r_1^{(2)} = {}^{(I)}r_0 + \sqrt{2}l_0 \begin{bmatrix} \cos(\frac{\pi}{4} + \theta_0) \\ \sin(\frac{\pi}{4} + \theta_0) \end{bmatrix} + \frac{l_1^{(2)}}{2} \begin{bmatrix} \cos(\theta_1^{(2)} + \theta_0) \\ \sin(\theta_1^{(2)} + \theta_0) \end{bmatrix} \quad (6)$$

where the left superscript I represents the related vector described in the inertial frame, and $l_i^{(1)}$ and $l_j^{(2)}$ are the lengths of link i in arm 1 and link j in arm 2.

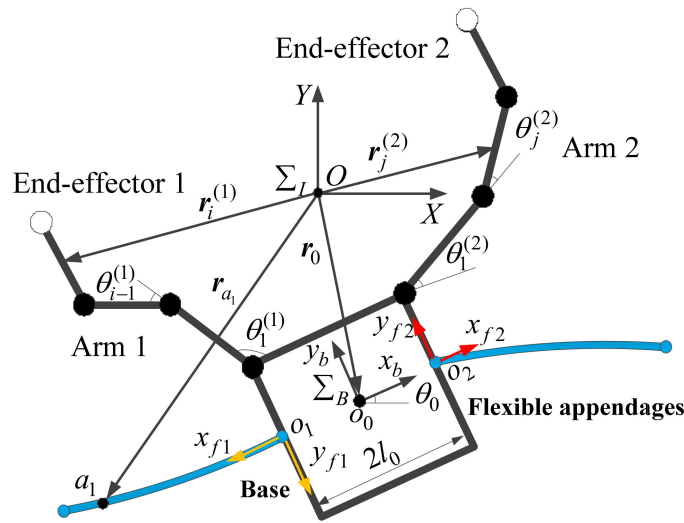


Figure 2. A dual-arm space robot with flexible appendages.

In this paper, the flexible appendages are simplified as two planar Euler–Bernoulli beam elements with small lateral deformation and no axial displacement. Hence, the generalized coordinates of a beam element, namely the deflection and rotation angle of boundary nodes, are given by:

$$q_{e1} = [0 \quad 0 \quad w_1 \quad \theta_{e1}]^T \tag{7}$$

where w_1 is the deflection of the tip of the beam. The rotation angle of the tip denoted by θ_{e1} is given by:

$$\theta_{e1} = \frac{\partial w_1}{\partial x} \tag{8}$$

where x is the element coordinate. The position vector of an arbitrary point a_1 on the beam in the local frame is expressed using a Hermite interpolation polynomial scheme as a shape function, as follows:

$${}^{(f1)}r_{x1} = [x_1 \quad w_{x1}] = [x_1 \quad N_{e1}q_{e1}] \tag{9}$$

$$N_{e1} = \left[1 - \frac{3x_1^2}{l_1^2} + \frac{2x_1^3}{l_1^3} \quad x_1 - \frac{2x_1^2}{l_1} + \frac{x_1^3}{l_1^2} \quad \frac{3x_1^2}{l_1^2} - \frac{2x_1^3}{l_1^3} \quad -\frac{x_1^2}{l_1} + \frac{x_1^3}{l_1^2} \right] \tag{10}$$

where l_1 is the length of beam element 1 and the left superscript f_1 indicates the corresponding vector expressed in the local frame of appendage 1. The location vector of an arbitrary point on the flexible appendage 1 expressed in the inertial frame is:

$${}^{(I)}r_{a1} = [x_{a1} \quad y_{a1}]^T = {}^{(I)}r_0 + R_0R_1([l_0 \quad 0]^T + {}^{(f1)}r_{x1}) \tag{11}$$

where R_0 and R_1 denote the transformation matrices from the base frame to the inertial frame and from the local frame of the appendage 1 to the base frame. Analogously, the position vector of an arbitrary point on the other flexible appendage is given as:

$${}^{(I)}r_{a2} = [x_{a2} \quad y_{a2}]^T = {}^{(I)}r_0 + R_0([l_0 \quad 0]^T + {}^{(f2)}r_{x2}) \tag{12}$$

$${}^{(f2)}r_{x2} = [x_2 \quad w_{x2}]^T = [x_2 \quad N_{e2}q_{e2}]^T \tag{13}$$

As shown in Figure 3, the modular component is equivalently modeled as a new virtual link with the same length, l_{v1} , and connected with end-effector 1 at its midpoint in width. Likewise, the length of virtual link 2, l_{v2} , can be obtained.

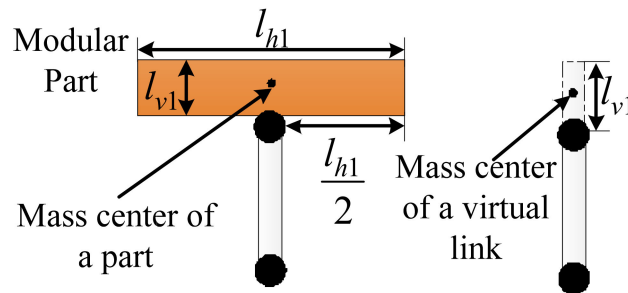


Figure 3. A modular part transformed to a virtual link.

The kinetic and potential energy of the system can be derived as follows:

$$T = T_b + T_m + T_f \tag{14}$$

$$T_f = \frac{1}{2} \int_0^{l_1} \rho_1^{(I)} \dot{\mathbf{r}}_{a1}^{(I)\top} \dot{\mathbf{r}}_{a1}^{(I)} dx + \frac{1}{2} \int_0^{l_2} \rho_2^{(I)} \dot{\mathbf{r}}_{a2}^{(I)\top} \dot{\mathbf{r}}_{a2}^{(I)} dx \tag{15}$$

$$T_{m1} = \frac{1}{2} \sum_{i=1}^{n_1} (m_i^{(I)} \dot{\mathbf{r}}_i^{(1)\top} \dot{\mathbf{r}}_i^{(1)} + (\omega_i^{(1)})^\top I_i \omega_i^{(1)}) \tag{16}$$

$$T_{m2} = \frac{1}{2} \sum_{j=1}^{n_2} (m_j^{(I)} \dot{\mathbf{r}}_j^{(2)\top} \dot{\mathbf{r}}_j^{(2)} + (\omega_j^{(2)})^\top I_j \omega_j^{(2)}) \tag{17}$$

$$T_b = \frac{1}{2} m_0^{(I)} \dot{\mathbf{r}}_0^{(I)\top} \dot{\mathbf{r}}_0^{(I)} + \frac{1}{2} I_0 \dot{\theta}_0^2 \tag{18}$$

$$V = \int_0^{l_1} \boldsymbol{\varepsilon}_1^\top \boldsymbol{\sigma}_1 dx + \int_0^{l_2} \boldsymbol{\varepsilon}_2^\top \boldsymbol{\sigma}_2 dx = \int_0^{l_1} \boldsymbol{\varepsilon}_1^\top \mathbf{D}_1 \boldsymbol{\varepsilon}_1 dx + \int_0^{l_2} \boldsymbol{\varepsilon}_2^\top \mathbf{D}_2 \boldsymbol{\varepsilon}_2 dx = \frac{1}{2} (\boldsymbol{\delta})^\top \mathbf{K}_e \boldsymbol{\delta} \tag{19}$$

$$\boldsymbol{\delta} = [w_1 \quad \theta_{e1} \quad w_2 \quad \theta_{e2}]^\top \tag{20}$$

where T_f , T_{m1} , T_{m2} , and T_b are the kinetic energy of flexible appendages, manipulators 1 and 2, and the base, V denotes the elastic potential energy of flexible appendages, ρ_1 , ρ_2 and l_1 , l_2 represent the linear densities and lengths of the two beams, and m_i , I_i and m_j , I_j are the mass and rotary inertia of links i and j with respect to their mass centers in arms 1 and 2, respectively. $\omega_i^{(1)}$ and $\omega_j^{(2)}$ are the angular velocities of links i and j in arms 1 and 2, respectively. m_0 and I_0 denote the mass and rotary inertia of the base, and n_1 and n_2 indicate the degrees of freedom of arm 1 and arm 2, respectively. $\boldsymbol{\varepsilon}_1$ and $\boldsymbol{\varepsilon}_2$ as well as $\boldsymbol{\sigma}_1$ and $\boldsymbol{\sigma}_2$ are strains and stresses of the two arbitrary points on the two beams, and \mathbf{D}_1 and \mathbf{D}_2 denote the elastic matrices of the beams. Finally, $\mathbf{x}_0 = [{}^{(I)}\mathbf{r}_0^\top \quad \theta_0]^\top$, $\boldsymbol{\theta} = [\theta_1^{(1)} \quad \dots \quad \theta_{n_2}^{(2)}]^\top$, and $\boldsymbol{\delta}$ are treated as generalized coordinates. With the help of the Lagrange equations of the second kind, the dynamic equations of the system can be given as:

$$\begin{bmatrix} \mathbf{H}_0 & \mathbf{H}_{0m} & \mathbf{H}_{0\delta} \\ \mathbf{H}_{0m}^\top & \mathbf{H}_m & \mathbf{C}_{m\delta} \\ \mathbf{H}_{0\delta}^\top & \mathbf{C}_{m\delta}^\top & \mathbf{H}_\delta \end{bmatrix} \begin{bmatrix} \ddot{\mathbf{x}}_0 \\ \ddot{\boldsymbol{\theta}} \\ \ddot{\boldsymbol{\delta}} \end{bmatrix} + \begin{bmatrix} \mathbf{C}_0 & \mathbf{C}_{0m} & \mathbf{C}_{0\delta} \\ \mathbf{C}_{m0} & \mathbf{C}_m & \mathbf{C}_{m\delta} \\ \mathbf{C}_{\delta 0} & \mathbf{C}_{\delta m} & \mathbf{C}_\delta \end{bmatrix} \begin{bmatrix} \dot{\mathbf{x}}_0 \\ \dot{\boldsymbol{\theta}} \\ \dot{\boldsymbol{\delta}} \end{bmatrix} + \begin{bmatrix} \mathbf{0}_{3 \times 1} \\ \mathbf{0}_{(n_1+n_2) \times 1} \\ \mathbf{K}_e \boldsymbol{\delta} \end{bmatrix} = \begin{bmatrix} \mathbf{F}_0 \\ \boldsymbol{\tau} \\ \mathbf{0}_{4 \times 1} \end{bmatrix} \tag{21}$$

where \mathbf{F}_0 and $\boldsymbol{\tau}$ are generalized external force vectors applied on the base and manipulators and $\mathbf{0}_{3 \times 1}$ is a zero vector with three dimensions.

3. Two-Stage Control Scheme for Assembly

In the assembly mission, directly obtaining the final position and orientation of two modular components in the inertial frame would be difficult, making it challenging to accomplish one-step assembly. Hence, a two-stage strategy assembly scheme is introduced to assemble two modular components. In the first stage, the modular components reach their

relative preassembly positions and attitudes. Afterwards, the modular components follow a relative trajectory to achieve the final assembly. Moreover, the vibration of the flexible appendages induced by movements of the manipulators will bring about a disturbance force to the base, which poses significant effects for navigation and communication. The appendages lack external actuators, and the base is free-floating without the activated force, i.e., $F_0 = 0$. According to Equation (21), the generalized disturbance force generated by the movement of the manipulators can be obtained as:

$$F_{0m} = -(H_{0m}\ddot{\theta} + C_{0m}\dot{\theta}) \tag{22}$$

Accordingly, to reduce the disturbance force to the base and flexible appendages in the assembly operations, the disturbance force is involved in the optimal objective function.

3.1. Controller Design for the Preassembly Stage

This stage aims to carry the modular components to the desired preassembly position and attitude, as shown in Figure 4. A relative state between the components is selected as the desired state rather than the absolute defined values, which makes it applicable for both redundant and non-redundant robotic systems to operate the assembly task. Thereafter, relative movements are attained through a relative Jacobian matrix of the space robotic system. It is noted that the generalized relative Jacobian matrix expressed in the inertial frame becomes more sophisticated with the flexible appendages [13]. Accordingly, in this section, the relative motion is achieved in the base frame rather than the inertial frame, wherein only the relative Jacobian matrix as a substitute of the generalized one is required.

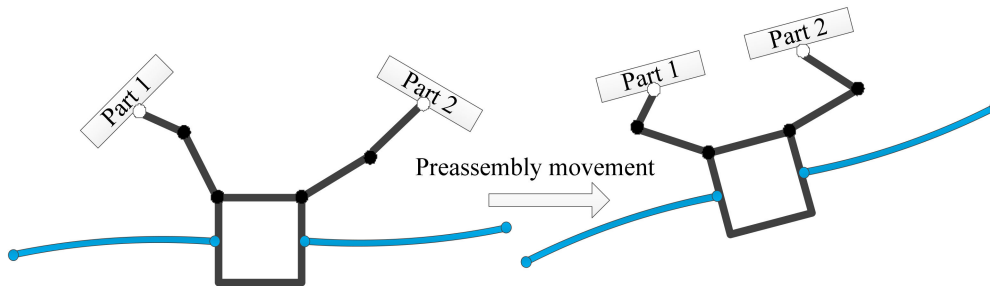


Figure 4. Preassembly to achieve the defined state.

Since the modular components are modeled as the virtual links, the issue is transformed to the motion control of two end-effectors. For further simplification, two virtual points in the end-effector frame are created to describe the relative position between the components, as depicted in Figure 5, where l_{h1} and l_{h2} are the widths of components 1 and 2, respectively. Thereafter, it is noted that only the relative distance between the components, l^r , is demanded rather than the relative position vector indicated in the base frame. Consequently, the current and desired relative states are obtained as:

$${}^{(B)}\mathbf{X}_{VP}^{(r)} = [{}^{(B)}\mathbf{x}_{VP}^{(r)} \quad \theta^{(r)}]^T \tag{23}$$

$${}^{(B)}\mathbf{x}_{VP}^{(r)} = {}^{(B)}\mathbf{x}_{VP2} - {}^{(B)}\mathbf{x}_{VP1}, \quad \theta^{(r)} = {}^{(B)}\theta_{P2} - {}^{(B)}\theta_{P1} \tag{24}$$

$${}^{(B)}\mathbf{X}_{D1}^{(r)} = [0 \quad 0 \quad \theta_d^{(r)}]^T \tag{25}$$

where the right superscript r represents the relative value concerning the position coordinate and attitude angle, ${}^{(B)}\mathbf{x}_{VP1}$ and ${}^{(B)}\mathbf{x}_{VP2}$ are the current positions of two virtual points in the base frame, ${}^{(B)}\theta_{P1}$ and ${}^{(B)}\theta_{P2}$ denote the current attitudes of two virtual links, namely two modular components in Euler angles expressed in the base frame, and θ_d^r represents the

desired rotation angle between the virtual links. Then, the relative velocity and acceleration are expressed as follows:

$${}^{(B)}\dot{\mathbf{X}}_{VP}^{(r)} = \begin{bmatrix} {}^{(B)}\dot{\mathbf{x}}_{VP2} - {}^{(B)}\dot{\mathbf{x}}_{VP1} \\ {}^{(B)}\dot{\theta}_{P2} - {}^{(B)}\dot{\theta}_{P1} \end{bmatrix} = {}^{(B)}\mathbf{J}_{VP}^{(r)}\dot{\theta} \tag{26}$$

$${}^{(B)}\ddot{\mathbf{X}}_{VP}^{(r)} = {}^{(B)}\mathbf{J}_{VP}^{(r)}\ddot{\theta} + {}^{(B)}\dot{\mathbf{J}}_{VP}^{(r)}\dot{\theta} \tag{27}$$

where ${}^{(B)}\dot{\mathbf{x}}_{VP1}$ and ${}^{(B)}\dot{\mathbf{x}}_{VP2}$ are the linear velocities of virtual points 1 and 2, respectively, ${}^{(B)}\dot{\theta}_{P1}$ and ${}^{(B)}\dot{\theta}_{P2}$ are the angular velocities of virtual links 1 and 2, respectively, and ${}^{(B)}\mathbf{J}_{VP}^{(r)}$ is a combined relative Jacobian matrix defined in the base frame.

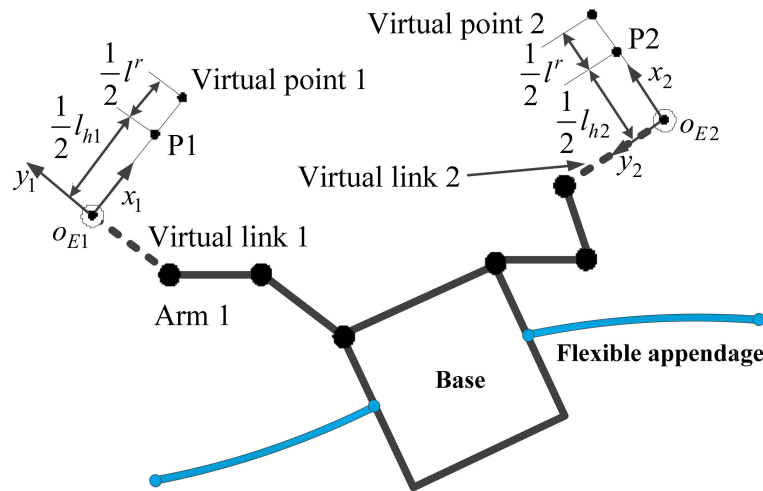


Figure 5. Virtual points created in the preassembly stage.

According to the strategy, an optimal formula is established in which a transitional vector is adopted as the optimized variable to represent the joint acceleration and bounds in the amplitude of joint torques are taken into account through a dynamic equation constraint. Eventually, the optimal problem in a discrete-time form is given as follows:

$$\begin{aligned} & \underset{\mathbf{b}_k}{\text{minimize}} \quad \left\| {}^{(B)}\ddot{\mathbf{X}}_{VPk}^{(r)} - {}^{(B)}\mathbf{X}_{d1k}^{(r)} \right\|^2 + \|\mathbf{F}_{0mk}\|^2 \\ & \text{subject to} \quad |\tau_k| \leq \tau_{\max} \\ & \quad \quad \quad \ddot{\theta}_k = \mathbf{b}_k - \varepsilon_1 \dot{\theta}_k \\ & \quad \quad \quad {}^{(B)}\mathbf{X}_{d1k}^{(r)} = \varepsilon_2 ({}^{(B)}\mathbf{X}_{D1}^{(r)} - {}^{(B)}\mathbf{X}_{VP1k}^{(r)}) \\ & \quad \quad \quad \mathbf{H}(\theta_k, \dot{\theta}_k, \ddot{\theta}_k, \tau_k) = \mathbf{0} \end{aligned} \tag{28}$$

where the subscript k represents the vector at instant k , the item $\varepsilon_1 \dot{\theta}_k$ is added to avoid the joint velocity oscillation, ε_1 and ε_2 are two constant coefficients concerning the convergence rate, and $\mathbf{H}(\theta_k, \dot{\theta}_k, \ddot{\theta}_k, \tau_k)$ denotes the dynamics constraint indicated in Equation (21). Once the optimized variable \mathbf{b}_k is solved, the demanded joint acceleration is obtained. Then, the joint torques as a control input is calculated through the inverse dynamics of the robotics system.

3.2. Controller Design for the Trajectory Tracking Stage

At the end of preassembly stage, two modular components reached the desired relative position and attitude, as shown in Figure 6, where P1 and P2 are two points of modular components 1 and 2, respectively. It is noted that the strategy for driving the single arm to accomplish the final assembly brings about an obvious disturbance force to the base, despite moving in a small scope [13]. Hence, in this stage, components 1 and 2 are carried

following a relative trajectory between P1 and P2, while the attitude of component 2 with respect to component 1 should remain unchanged. At the same time, the disturbance force is added to the optimal objective function. The relative velocity between the components is defined as:

$${}^{(B)}\dot{\mathbf{X}}_P^{(r)} = \begin{bmatrix} {}^{(B)}\dot{x}_{P2} - {}^{(B)}\dot{x}_{P1} \\ {}^{(B)}\dot{\theta}_{P2} - {}^{(B)}\dot{\theta}_{P1} \end{bmatrix} = {}^{(B)}\mathbf{J}_P^{(r)} \dot{\boldsymbol{\theta}} \tag{29}$$

$${}^{(B)}\ddot{\mathbf{X}}_P^{(r)} = {}^{(B)}\mathbf{J}_P^{(r)} \ddot{\boldsymbol{\theta}} + {}^{(B)}\dot{\mathbf{J}}_P^{(r)} \dot{\boldsymbol{\theta}} \tag{30}$$

$${}^B\dot{\mathbf{X}}_D = \left[\varepsilon_3 \left({}^{(B)}x_{P2} - {}^{(B)}x_{P1} \right) \quad 0 \right]^T \tag{31}$$

where ε_3 is a constant coefficient regarding convergence, ${}^{(B)}x_{P1}$ and ${}^{(B)}x_{P2}$ represent the positions of points P1 and P2 in the base frame, respectively, ${}^{(B)}\dot{x}_{P1}$ and ${}^{(B)}\dot{x}_{P2}$ are the linear velocities of components 1 and 2, respectively, and ${}^{(B)}\mathbf{J}_P^{(r)}$ denotes the relative Jacobian matrix of the two modular components. To achieve the relative trajectory tracking and reduce the disturbance force to the base, an optimal problem is formulated as follows:

$$\begin{aligned} & \underset{c_k}{\text{minimize}} \quad \left\| {}^B\ddot{\mathbf{X}}_{Pk}^{(r)} - {}^B\mathbf{X}_{d2k}^{(r)} \right\|^2 + \|F_{0mk}\|^2 \\ & \text{subject to} \quad |\tau_k| \leq \tau_{\max} \\ & \quad \quad \quad \dot{\boldsymbol{\theta}}_k = c_k - \varepsilon_1 \dot{\boldsymbol{\theta}}_k \\ & \quad \quad \quad {}^B\mathbf{X}_{d2k}^{(r)} = \varepsilon_4 ({}^B\dot{\mathbf{X}}_{D2k} - {}^B\dot{\mathbf{X}}_{Pk}^{(r)}) \\ & \quad \quad \quad H(\boldsymbol{\theta}_k, \dot{\boldsymbol{\theta}}_k, \ddot{\boldsymbol{\theta}}_k, \tau_k) = \mathbf{0} \end{aligned} \tag{32}$$

where c_k is a new variable to represent the control input.

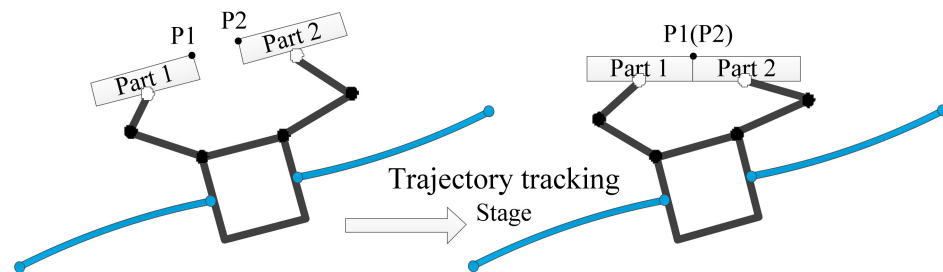


Figure 6. Trajectory tracking stage for the final assembly.

4. Simulation Results

In this section, the proposed assembly strategy is validated for a space robot with two three-DOF arms and flexible appendages. The physical parameters of the robot and modular components are presented in Table 1. The system was initially at rest, with the initial states of the joint and base shown in Table 2, where the inertial frame aligned with the base frame. The lengths of the beams, l_1 and l_2 , were selected as 3 m, and the linear densities of the beams ρ_1 and ρ_2 were set as 0.5 kg/m^3 . The desired rotation angle between two virtual links, ${}^B\theta_d^r$, was set as 0, and the relative distance, l^r , was chosen as 0.2 m. The coefficients $\varepsilon_1, \varepsilon_2, \varepsilon_3$, and ε_4 were 1, 0.2, 0.8, and 2. The maximum value of the joint torques was chosen as $2 \text{ N} \cdot \text{m}$. The simulation times of the preassembly and trajectory tracking stages were 20 s and 10 s, with a time step of 1 ms. The developed scheme was implemented via MATLAB (version R2014a) in the Windows 7 operation system on a desktop computer with an Intel i7 3.60 GHz CPU. The optimal problems were solved through a CVX toolbox with the default solver SDPT3 [28]. Once joint accelerations had been calculated, the joint velocities and angles were solved through a numerical integration using the fourth-order Runge–Kutta scheme.

Table 1. Robot physical properties.

	Mass (kg)	I_z (kg·m ²)	Dimension (m)
Base	20	3.33	1 × 1
Links 1, 3	5	0.833	1
Links 2, 4	5	0.533	0.5
Modular parts 1, 2	5	0.454	1 (l_{h1}) × 0.3 (l_{v1})

Table 2. Initial states of the robot system.

	Symbols (Unit)	Initial Conditions ($t = 0$)
Position of the base	r_0 (m)	$[0 \ 0 \ 0]^T$
Attitude of the base	R_0	Identity matrix
Joint angles of arm 1	θ_1 (rad)	$[\frac{3\pi}{4} \ 0 \ \frac{\pi}{4}]^T$
Joint angles of arm 2	θ_2 (rad)	$[\frac{\pi}{4} \ 0 \ -\frac{\pi}{4}]^T$

The simulation results in the preassembly stage are presented in Figures 7–16. One can see that the control inputs and joint velocities of the manipulators converged to zero after approximately 15 s, as shown in Figures 7 and 8, wherein the control inputs were under the demanded bounds. Figures 9 and 10 depict the mass center position and linear velocity of the base. Figures 11 and 12 demonstrate the angular velocity and rotation angle of the base, in which the maximum values were less than 2×10^{-6} and 5×10^{-5} , respectively. Moreover, comparison cases were carried out, where the UNOP was the case without a disturbance force item in the optimal objective function. The obvious optimal results of the deformation and rotation angle of the free tips on the beams are demonstrated in Figures 13 and 14, where the maximum values of the optimized deformation and rotation angle of the tips were less than 3×10^{-5} and 1.5×10^{-5} , respectively. As illustrated in Figures 15 and 16, at the end of this stage, the relative position error between two virtual points and the relative rotation angle between the two modular components converged to zero; that is, the modular components had achieved the expected relative state for the final assembly.

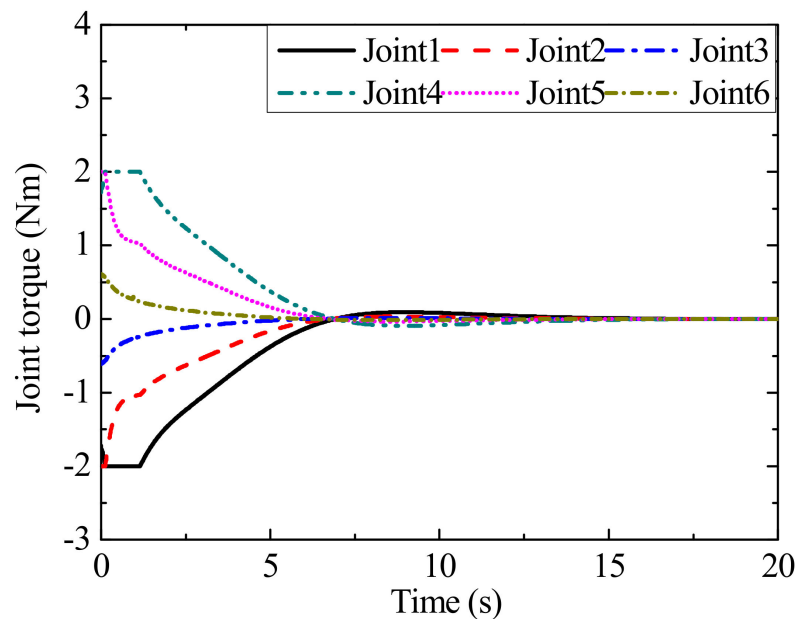


Figure 7. Control inputs in the preassembly stage.

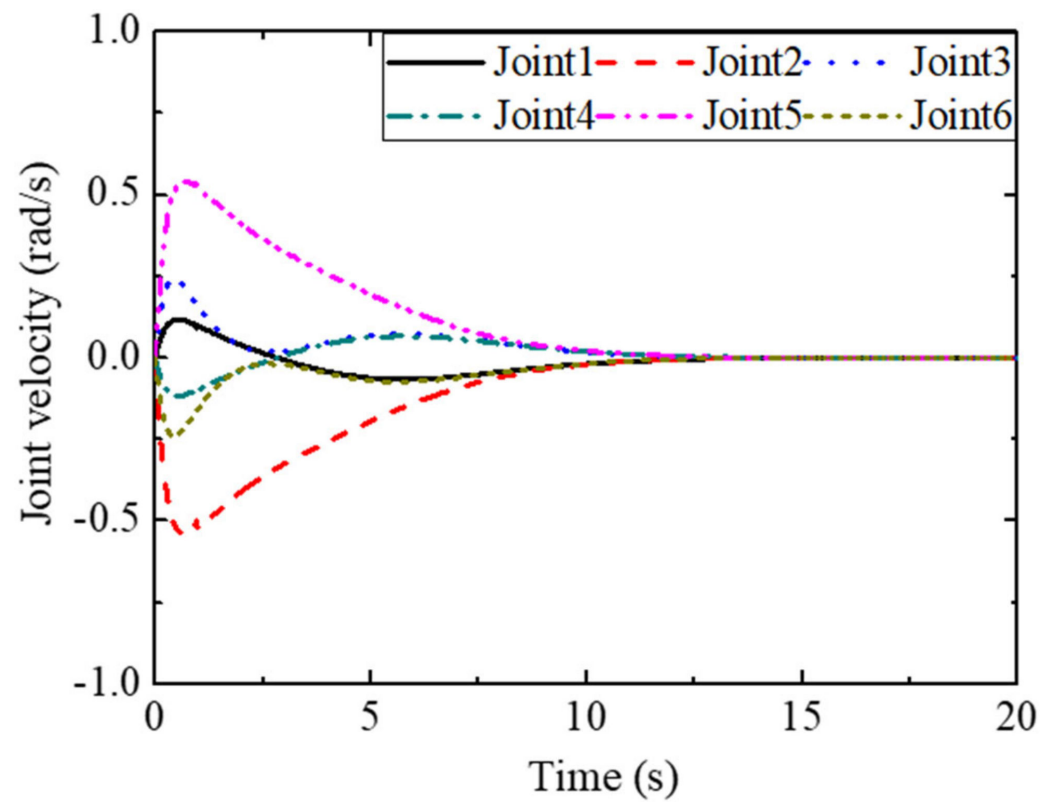


Figure 8. Joint velocities in the preassembly stage.

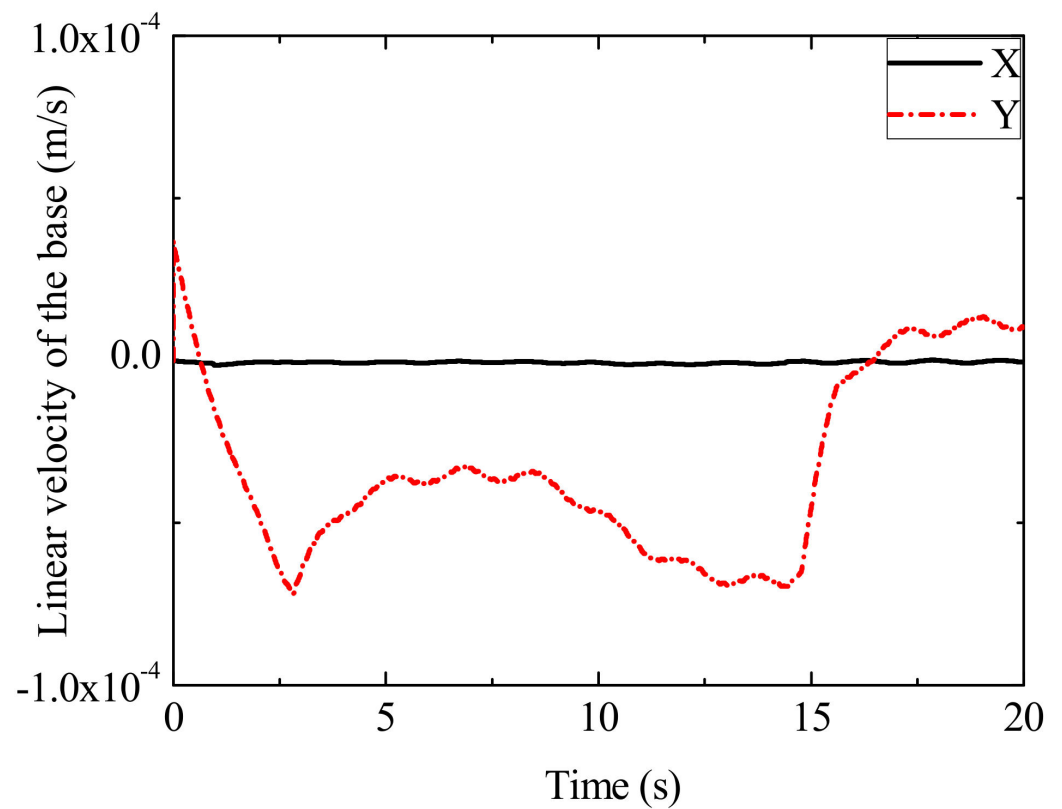


Figure 9. Linear velocity of the base in the preassembly stage.

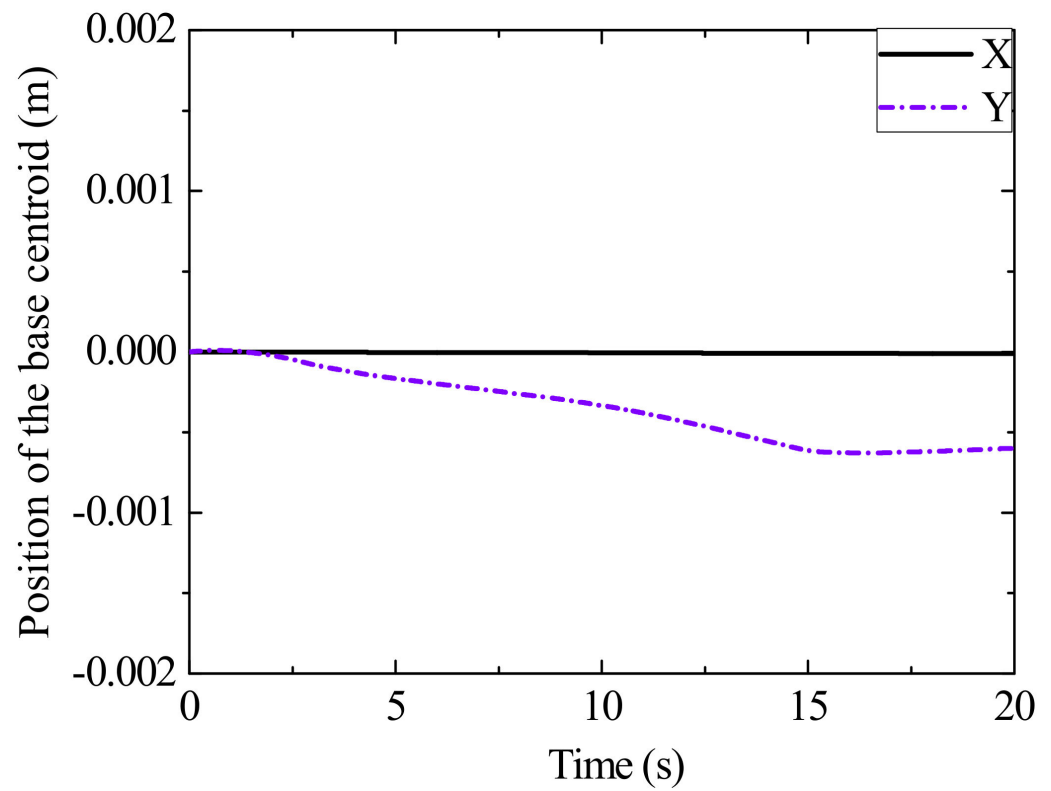


Figure 10. Position of the base centroid in the preassembly stage.

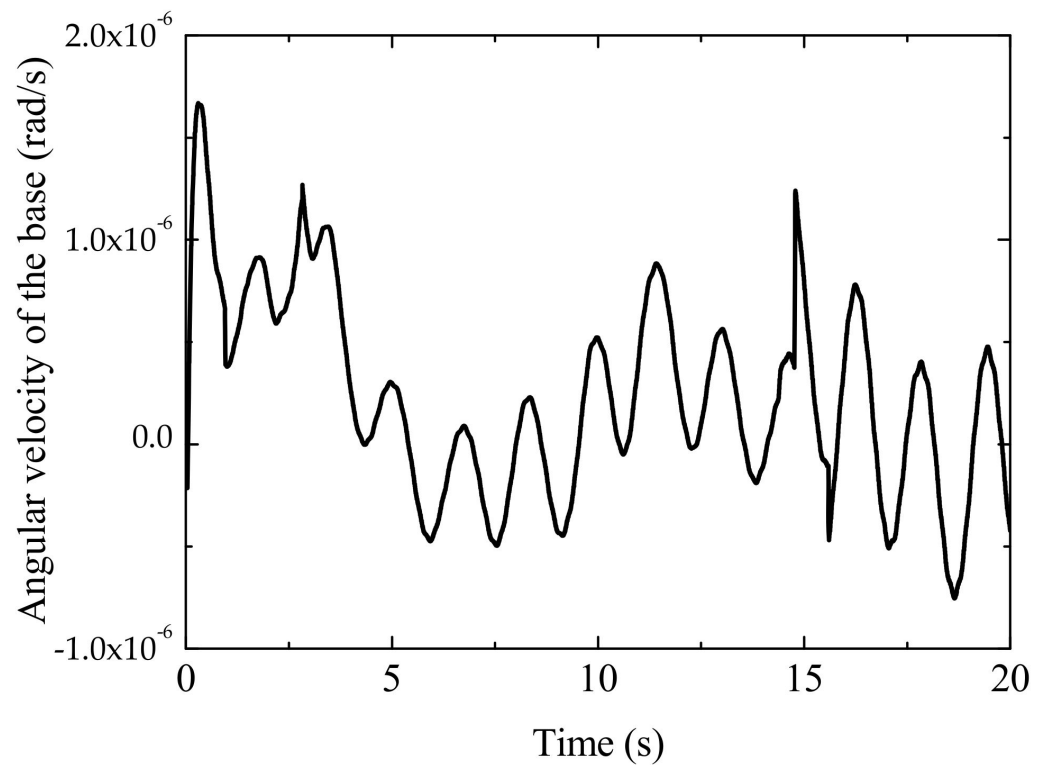


Figure 11. Angular velocity of the base in the preassembly stage.

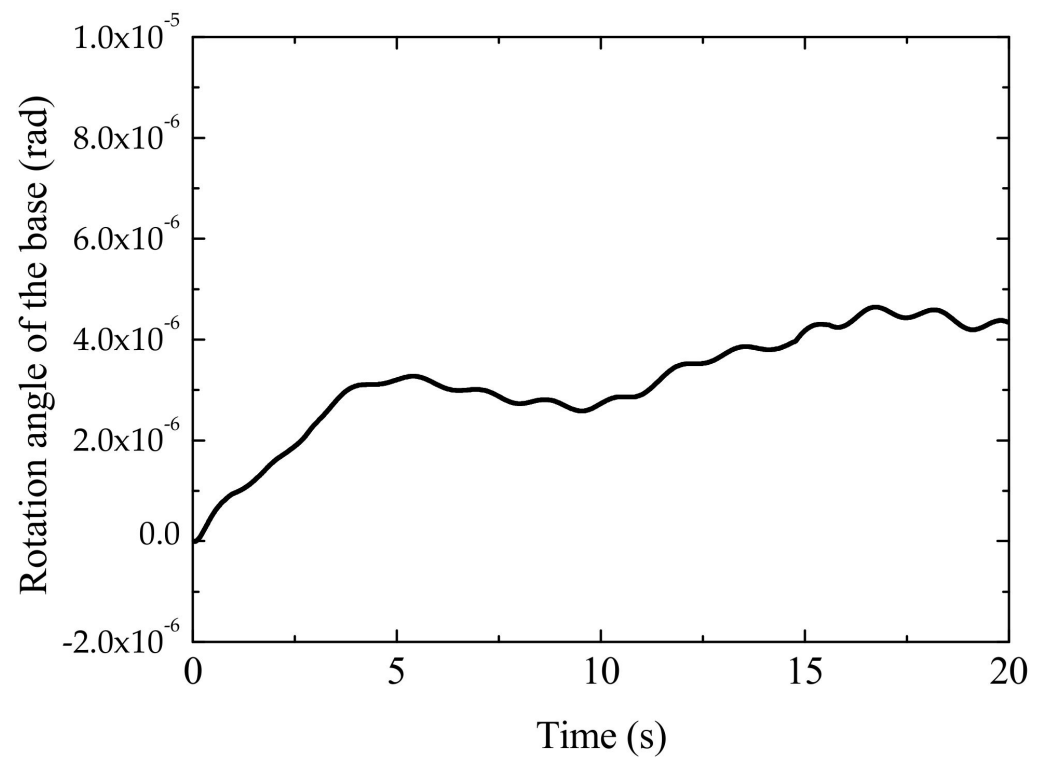


Figure 12. Rotation angle of the base in the preassembly stage.

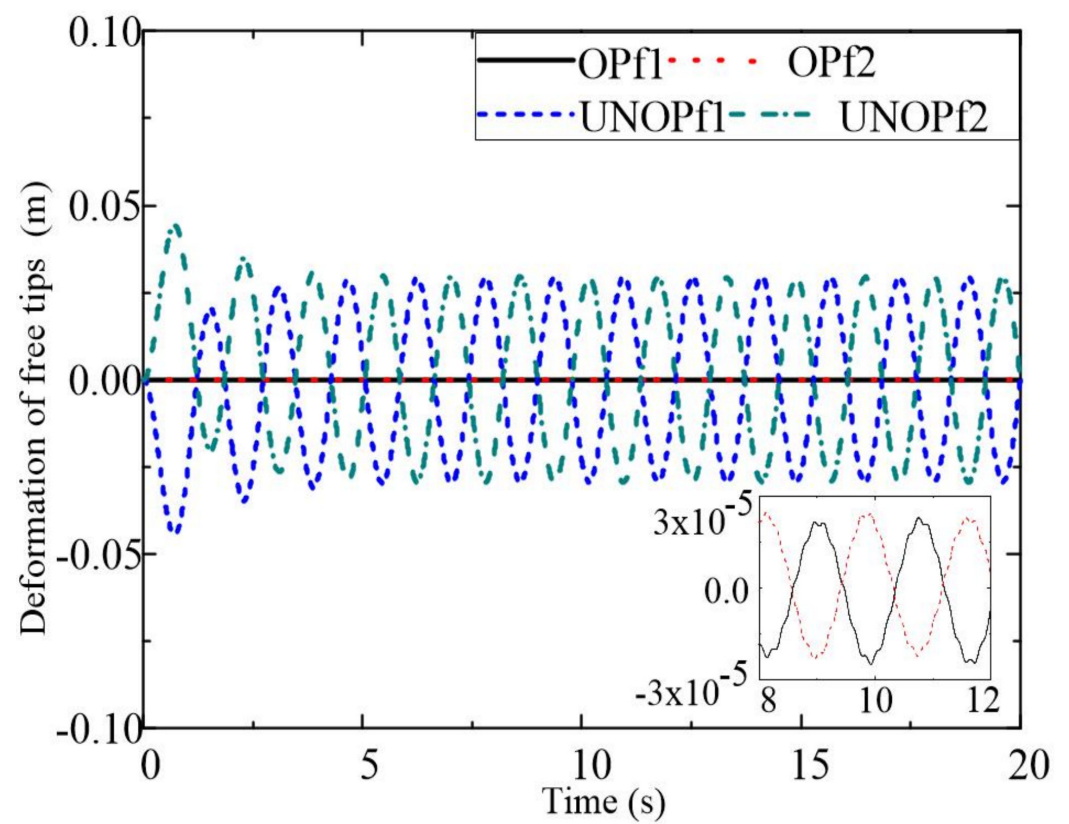


Figure 13. Deformation of the tips on the beams during the preassembly stage.

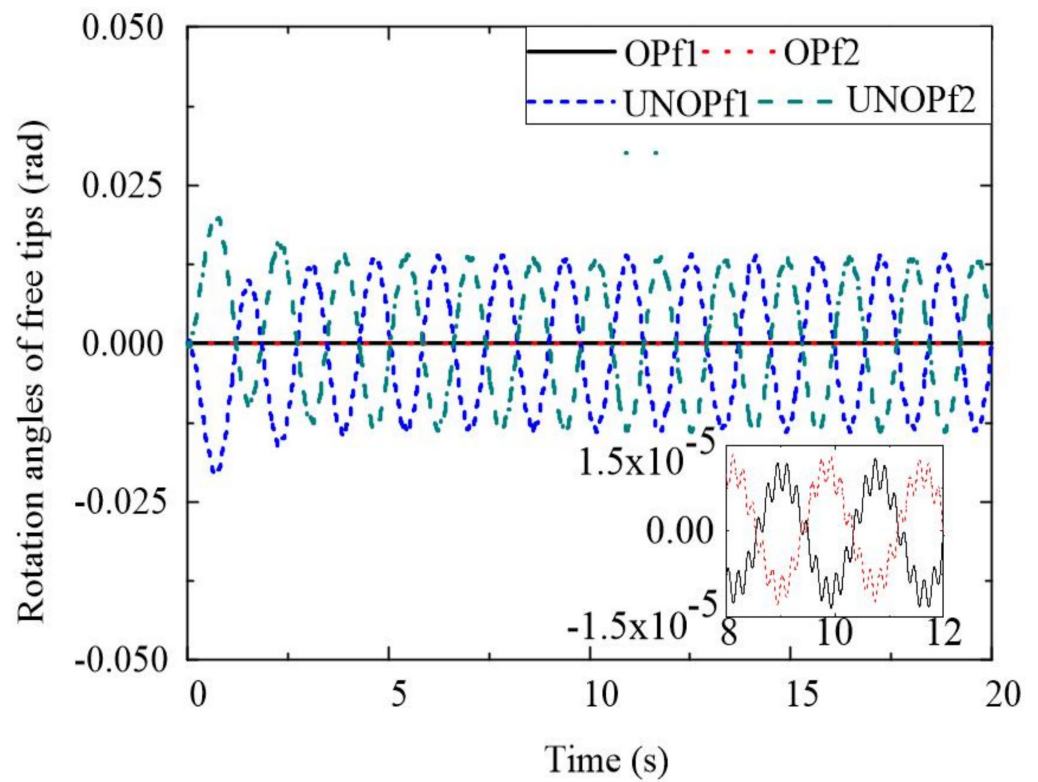


Figure 14. Rotation angles of the tips of the beams during the preassembly stage.

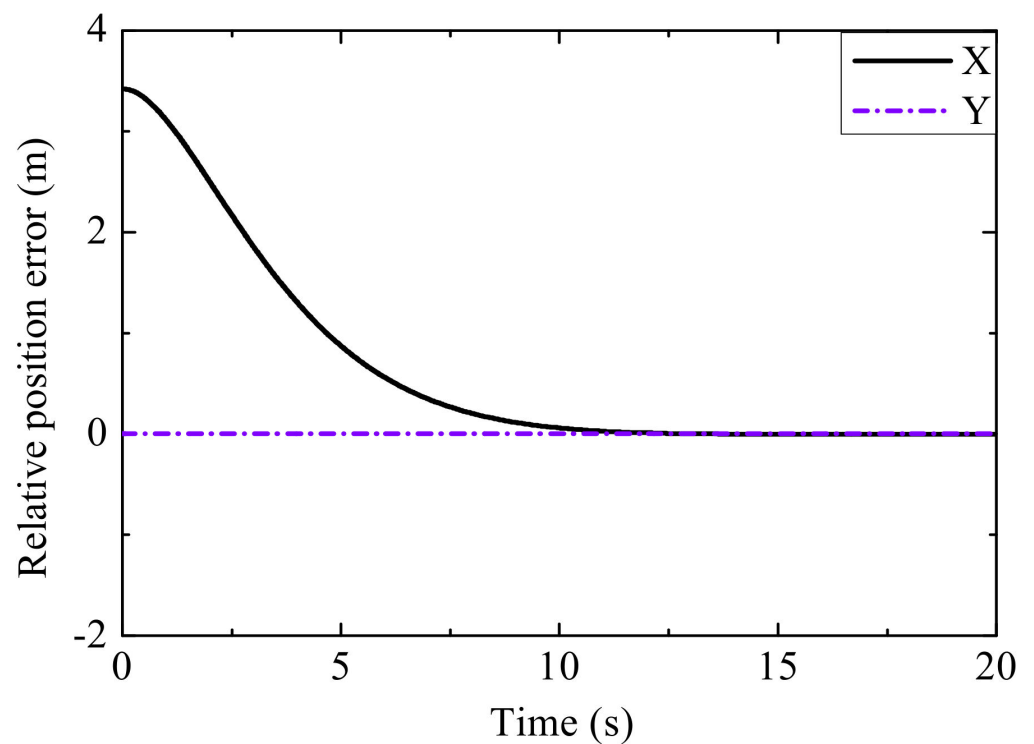


Figure 15. Relative position between two virtual points in the preassembly stage.

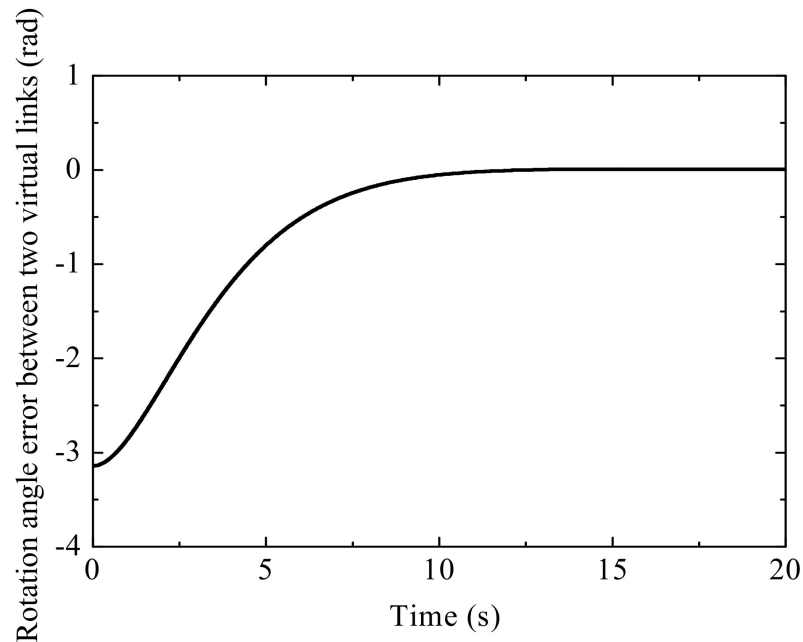


Figure 16. Relative attitude between the two modular components in the preassembly stage.

The simulation results in the trajectory tracking stage are shown in Figures 17–27. It can be seen from Figures 17 and 18 that the joint torques all satisfied the limitation and converged to zero along with the joint velocities at the end of the simulation. Figures 19–22 illustrate the center mass position and rotation angle of the base as well as their velocities. Besides, the deformation and rotation angle of the free tips on the beams are demonstrated in Figures 23 and 24, where the maximum values of the optimized deformation and rotation angle of the tips were less than 3×10^{-5} and 2×10^{-5} , respectively. As shown in Figures 25 and 26, the position error between P1 and P2 converged to zero and the relative attitude between the two components remained unchanged in this stage. In Figure 27, the trajectory of P2 in the local frame of component 1 is shown, and it indicates that P2 moved to P1 following the relative trajectory directed from P2 to P1. The complete trajectory of the robotic system is shown in Figure 28, wherein the modular components were successfully assembled in two stages.

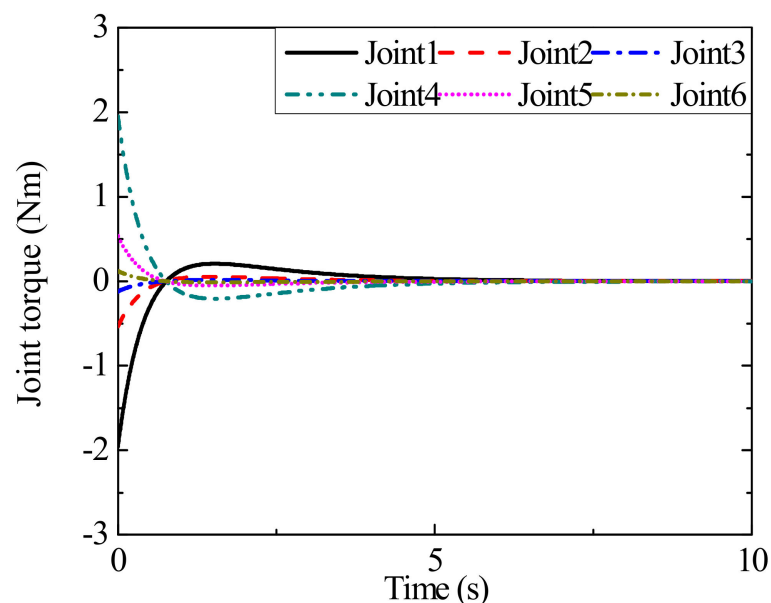


Figure 17. Control inputs in the trajectory tracking stage.

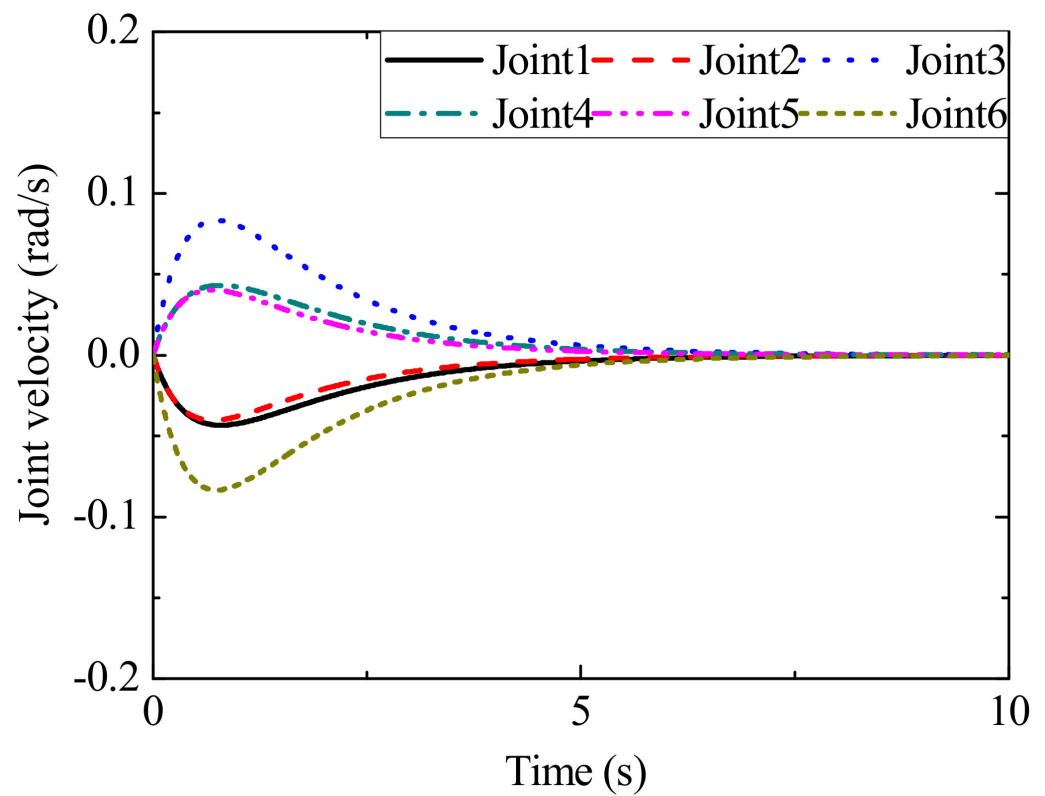


Figure 18. Joint velocities in the trajectory tracking stage.

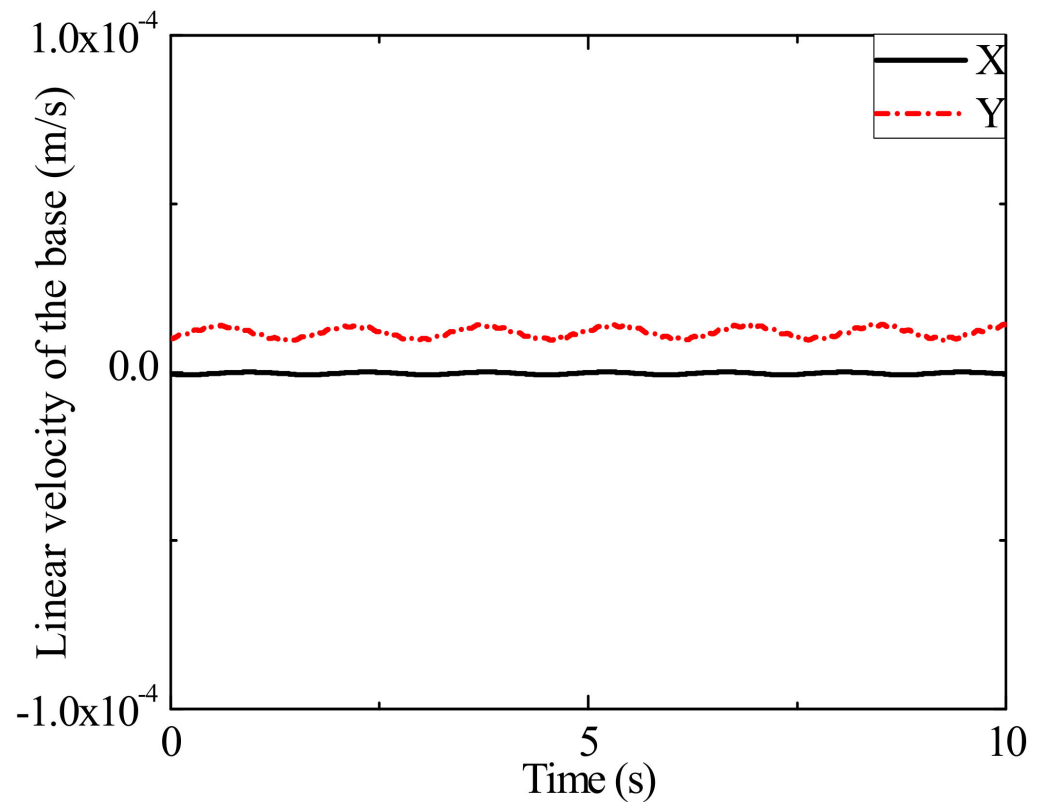


Figure 19. Linear velocity of the base in the trajectory tracking stage.

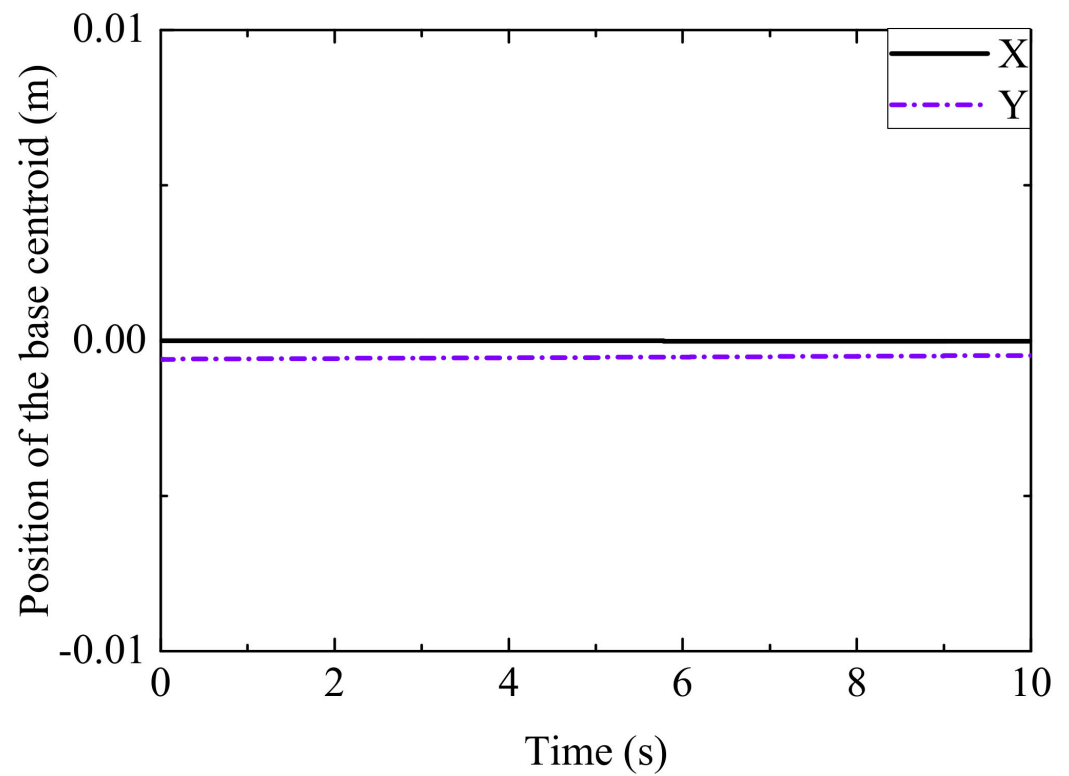


Figure 20. Position of the base centroid in the trajectory tracking stage.

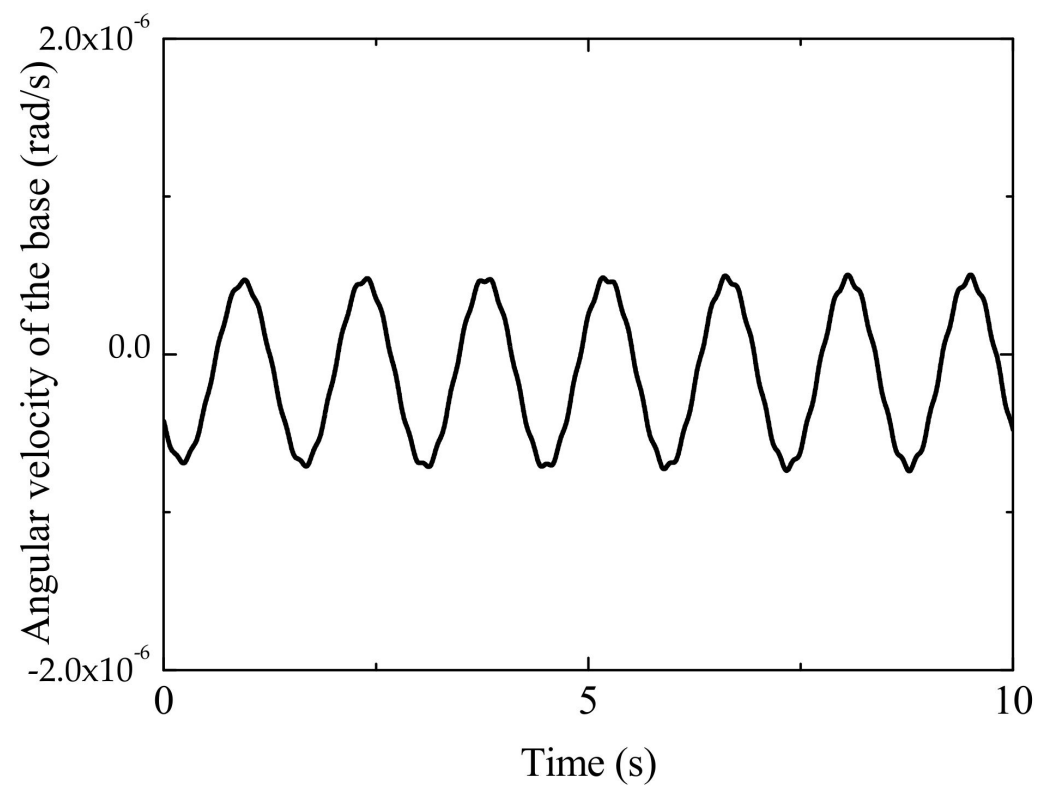


Figure 21. Angular velocity of the base in the trajectory tracking stage.

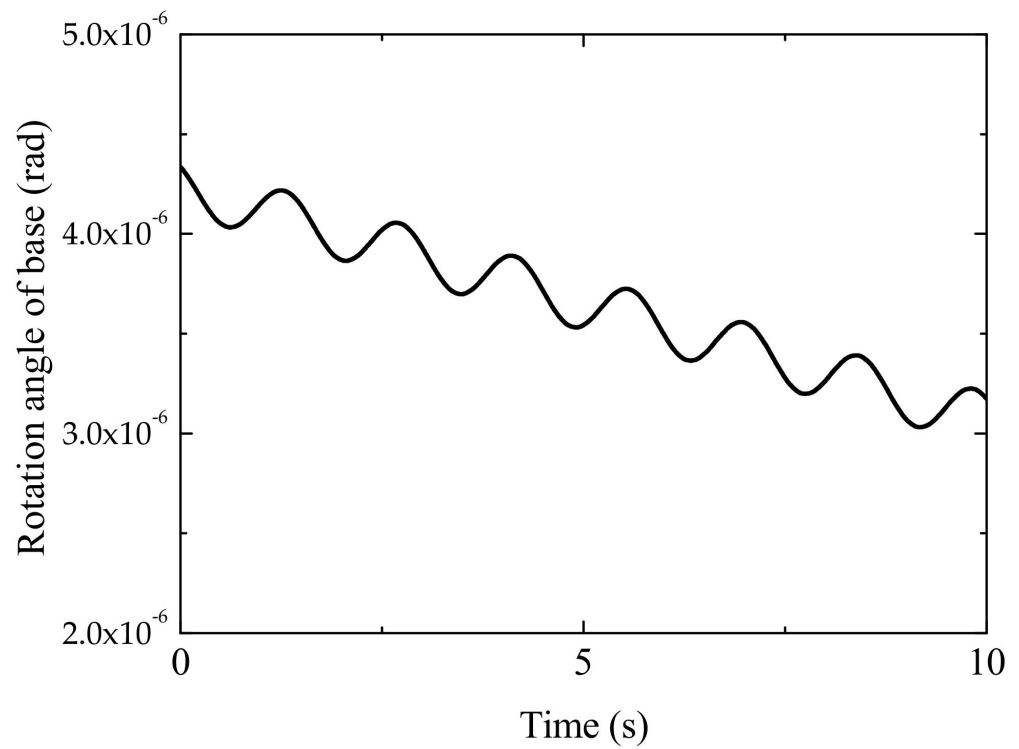


Figure 22. Rotation angle of the base in the trajectory tracking stage.

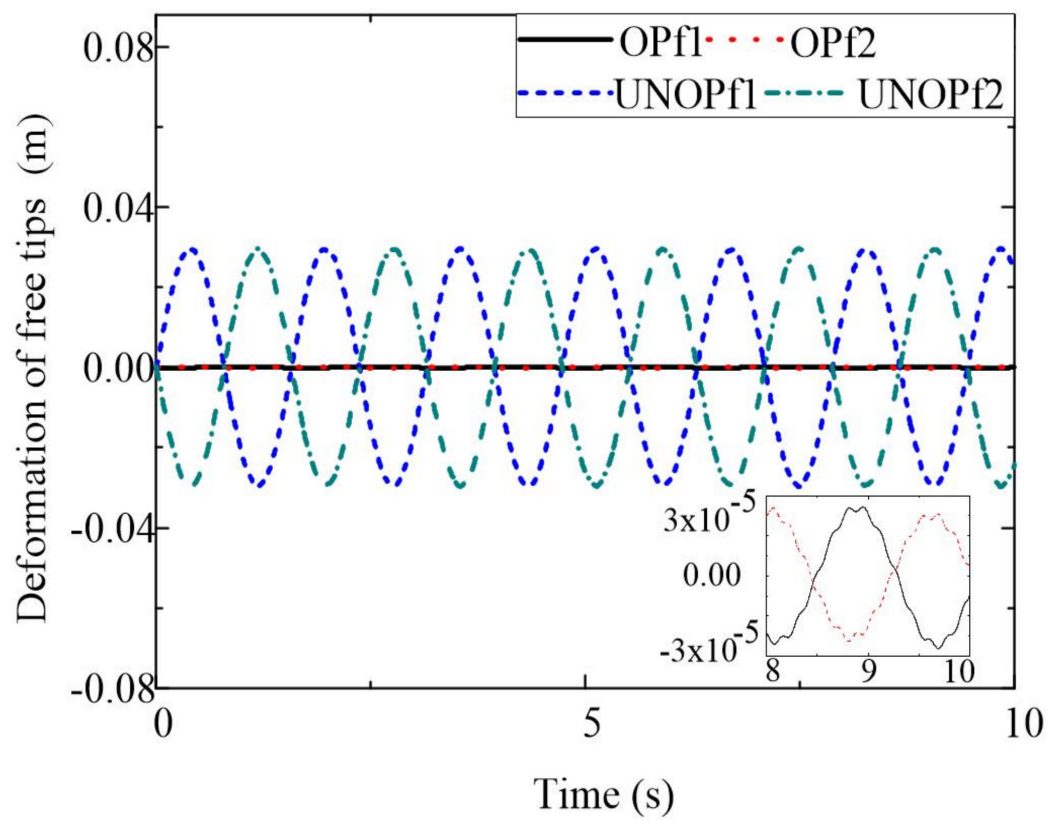


Figure 23. Deformation of the tips of the beams during the trajectory tracking stage.

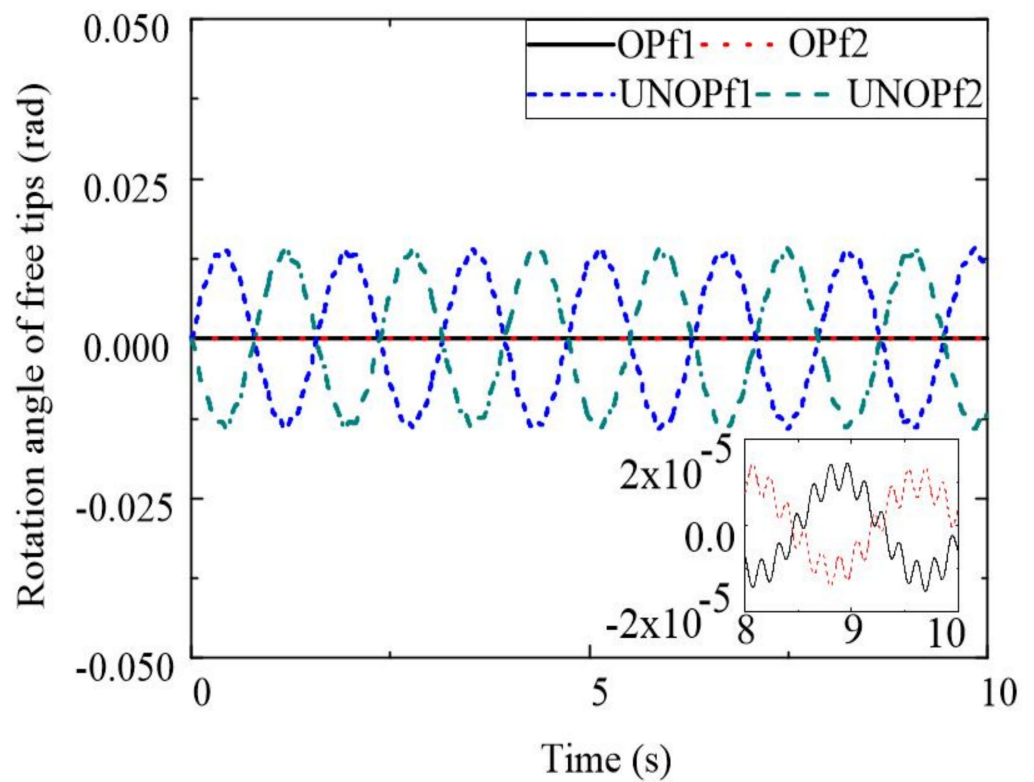


Figure 24. Rotation angles of the tips of the beams during the trajectory tracking stage.

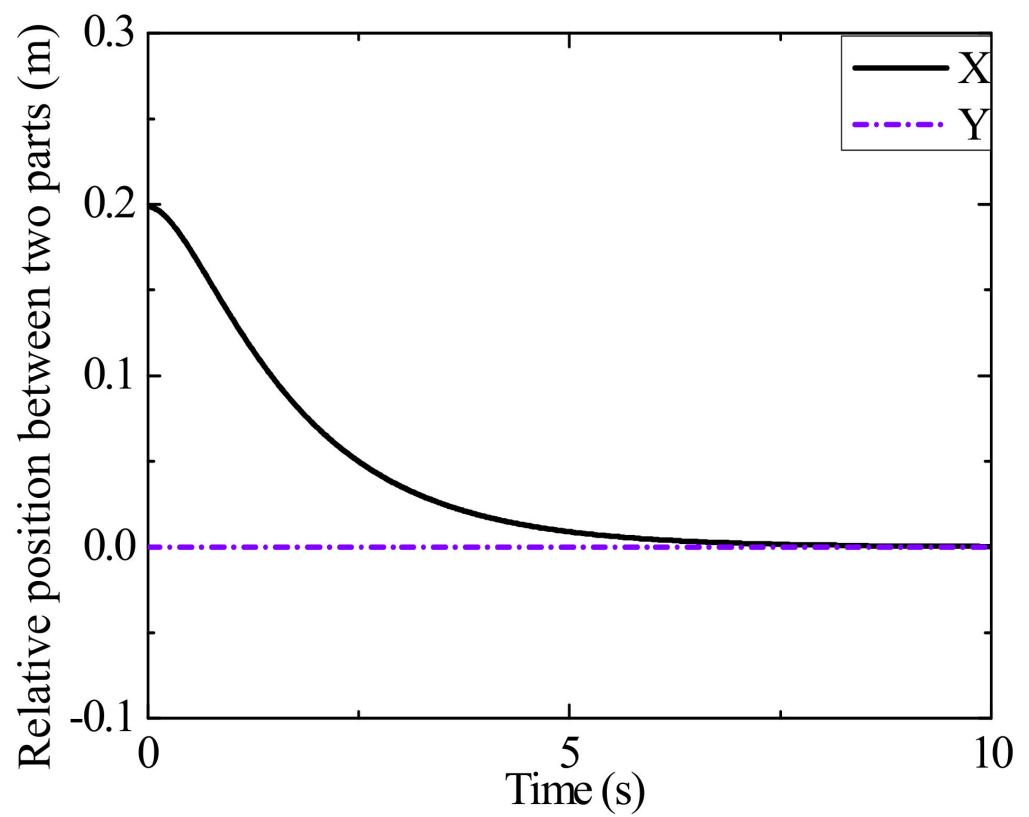


Figure 25. Relative position between the two modular components in the trajectory tracking stage.

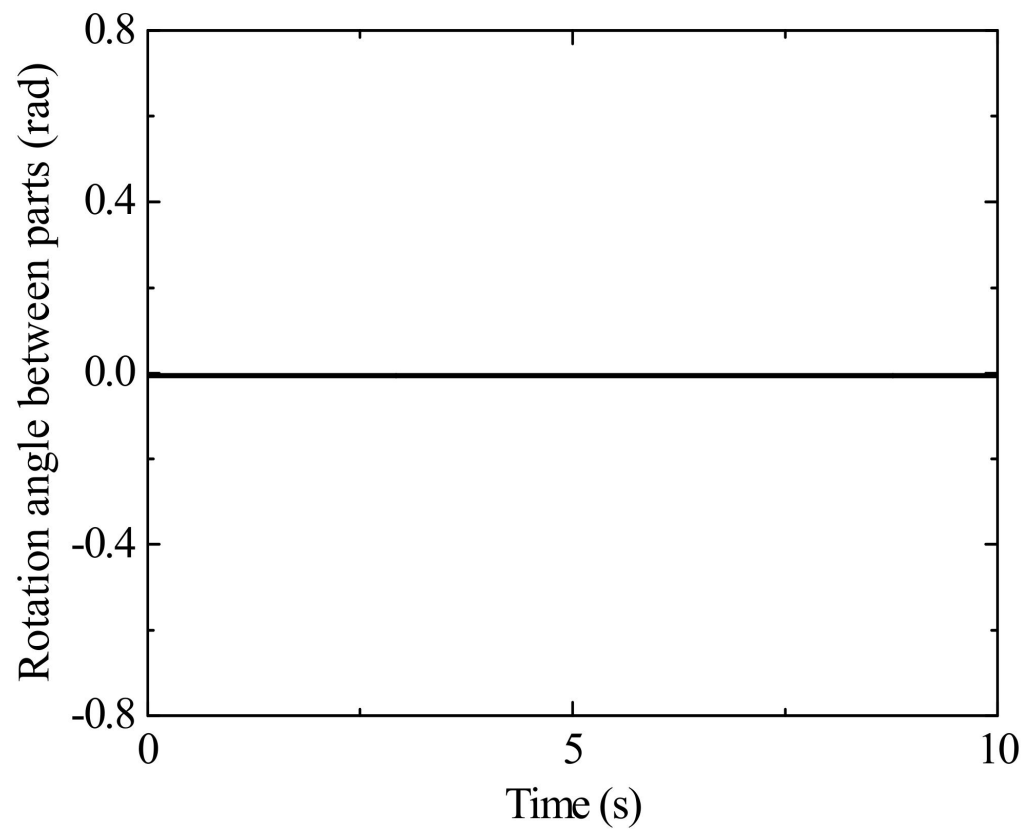


Figure 26. Relative attitude between the two modular components in the trajectory tracking stage.

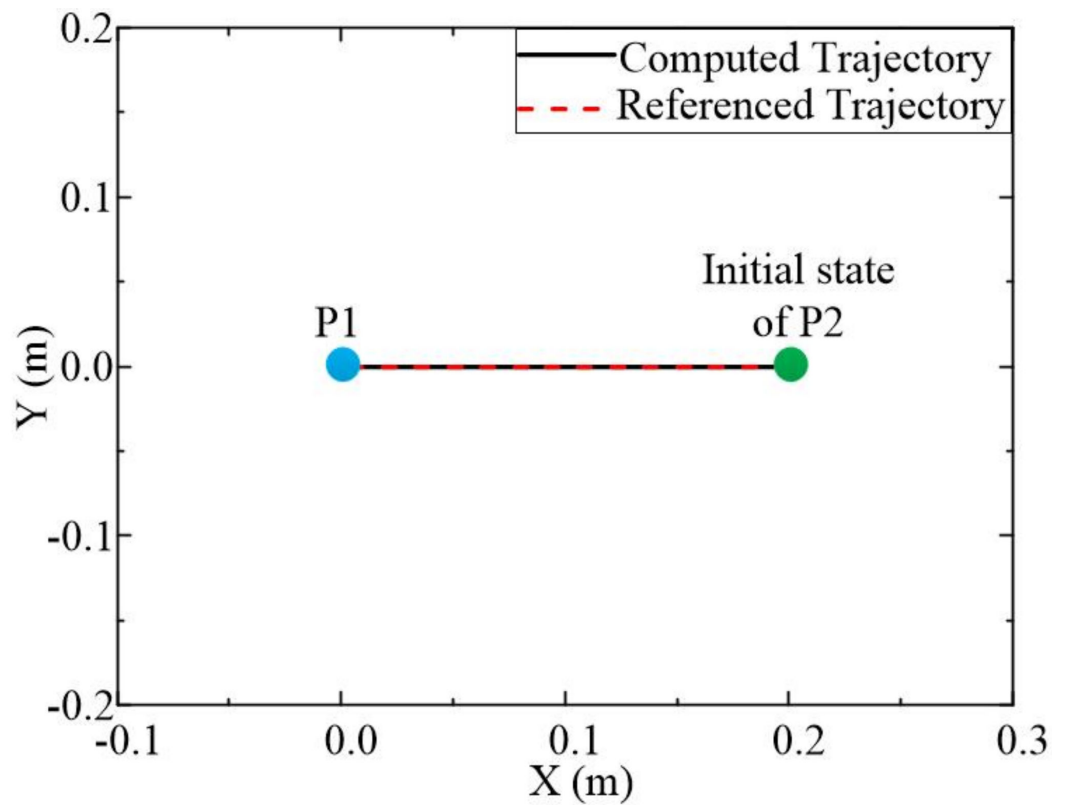


Figure 27. Trajectory of P2 in the end-effector 1 frame.

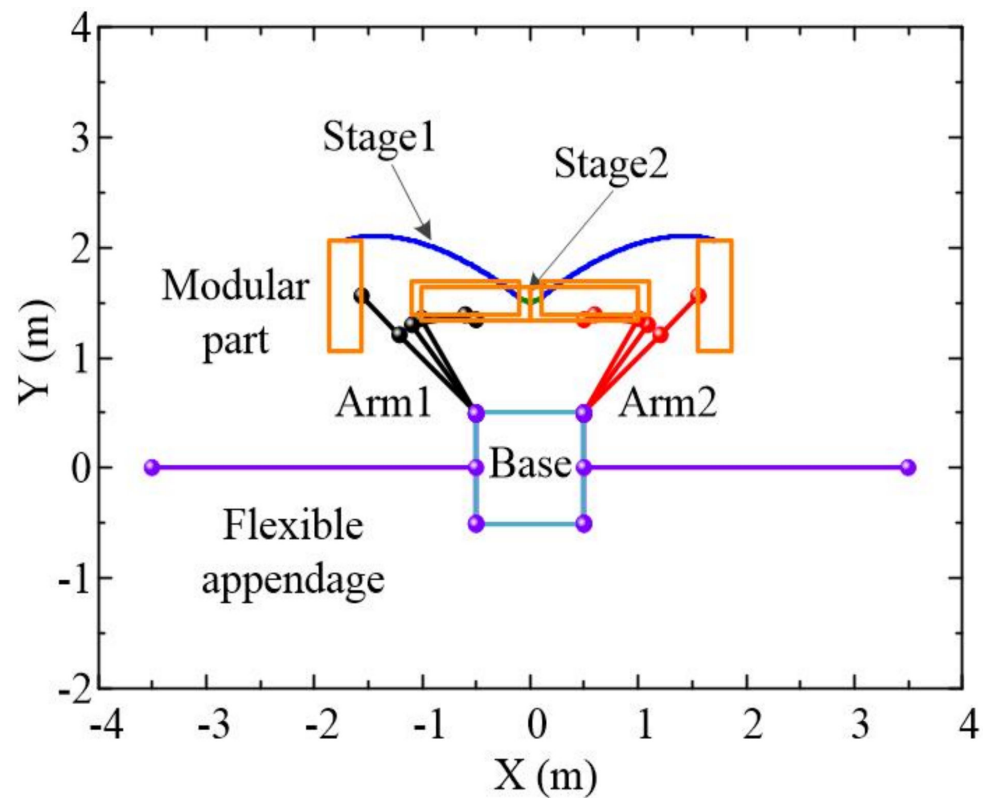


Figure 28. Trajectory of the robotic system in two stages.

5. Conclusions

In this paper, a two-stage strategy was proposed to assemble two modular components using a dual-arm space robot with flexible appendages. The dynamics model of the robotics system was established with Lagrange equations of the second kind. The assembly operation was performed based on the relative motion of the two modular components in the base frame and to minimize the disturbance force to the base and flexible appendages. More specially, the two components attained the desired relative position and attitude in the preassembly stage with the assistance of two virtual points. Furthermore, the components followed a relative trajectory for the final assembly by minimizing the relative velocity tracking error. Finally, the feasibility of the presented strategy was validated through numerical simulations of a robot with two three-DOF arms. The results demonstrated that the two-stage assembly scheme effectively achieved the goals in that the components firstly reached the desired relative states and then followed a desired trajectory with limits on the joint torque. Moreover, as a result of the optimization for the disturbance force, the response of the base and flexible appendages caused by movements of the manipulators was small enough to be ignored.

Author Contributions: Conceptualization, S.Y.; methodology, S.Y. and Y.Z.; supervision, T.C., H.W. and D.J. All authors have read and agreed to the published version of the manuscript.

Funding: This work was supported by the “14th Five-Year Plan” Civil Aerospace Pre-Research Project of China (D010301) and the National Natural Science Foundation of China (11832005 and 12102174).

Conflicts of Interest: The authors declare that they have no known competing financial interests or personal relationships that could have appeared to influence the work reported in this paper.

References

1. Moghaddam, B.M.; Chhabra, R. On the guidance, navigation and control of in-orbit space robotic missions: A survey and prospective vision. *Acta Astronaut.* **2021**, *184*, 70–100. [[CrossRef](#)]
2. Flores-Abad, A.; Ma, O.; Pham, K.; Ulrich, S. A review of space robotics technologies for on-orbit servicing. *Prog. Aerosp. Sci.* **2014**, *68*, 1–26. [[CrossRef](#)]
3. Qi, C.R.; Su, H.; Mo, K.; Guibas, L.J. Impact dynamic modelling and adaptive target capturing control for tethered space robots with uncertainties. *IEEE ASME Trans. Mechatron.* **2016**, *21*, 2260–2271. [[CrossRef](#)]
4. Mohan, S.; Miller, D.W. Dynamic Control Model Calculation: A Model Generation Architecture for Autonomous On-Orbit Assembly. *J. Spacecr. Rockets* **2014**, *51*, 1430–1453. [[CrossRef](#)]
5. Basmadj, F.L.; Seweryn, K.; Sasiadek, J.Z. Space robot motion planning in the presence of nonconserved linear and angular momenta. *Multibody Syst. Dyn.* **2020**, *50*, 71–96. [[CrossRef](#)]
6. Oegerle, W.R.; Purves, L.R.; Budinoff, J.G.; Moe, R.V.; Carnahan, T.M.; Evans, D.C.; Kim, C.K. Concept for a large scalable space telescope: In-space assembly. In Proceedings of the SPIE 6265, Space Telescopes and Instrumentation I: Optical, Infrared, and Millimeter, Orlando, FL, USA, 14 June 2006. [[CrossRef](#)]
7. Torisaka, A.; Hasegawa, S.; Miura, S.; Parque, V.; Miyashita, T.; Yamakawa, H.; Natori, M.C. Electromagnet-Based Three-Dimensional Self-Assembly System for Hierarchical Modular Space Structures. *J. Spacecr. Rockets* **2021**, *58*, 472–485. [[CrossRef](#)]
8. Pirat, C.; Ribes-Pleguezuelo, P.; Keller, F.; Marchi, A.Z.; Walker, R. Toward the Autonomous Assembly of Large Telescopes Using CubeSat Rendezvous and Docking. *J. Spacecr. Rockets* **2022**, *59*, 375–388. [[CrossRef](#)]
9. Gardner, J.P.; Mather, J.C.; Clampin, M.; Doyon, R.; Greenhouse, M.A.; Hammel, H.B.; Hutchings, J.B.; Jakobsen, P.; Lilly, S.J.; Long, K.S.; et al. The James Webb Space Telescope. *Sp. Sci. Rev.* **2006**, *123*, 485–606. [[CrossRef](#)]
10. Holub, V. Orb2: Spherical Space Station Designed for Single Launch and On-Orbit Assembly. *J. Spacecr. Rockets* **2021**, *58*, 708–714. [[CrossRef](#)]
11. Zappulla, R.; Virgili-Llop, J.; Zagaris, C.; Park, H.; Romano, M. Dynamic air-bearing hardware-in-the-loop testbed to experimentally evaluate autonomous spacecraft proximity maneuvers. *J. Spacecr. Rockets* **2017**, *54*, 825–839. [[CrossRef](#)]
12. Cao, K.; Li, S.; She, Y.; Biggs, J.D.; Liu, Y.; Bian, L. Dynamics and on-orbit assembly strategies for an orb-shaped solar array. *Acta Astronaut.* **2021**, *178*, 881–893. [[CrossRef](#)]
13. Yang, S.J.; Wen, H.; Hu, Y.H.; Jin, D.P. Coordinated motion control of a dual-arm space robot for assembling modular parts. *Acta Astronaut.* **2020**, *177*, 627–638. [[CrossRef](#)]
14. Staritz, P.J.; Skaff, S.; Urmson, C.; Whittaker, W. Skyworker: A robot for assembly, inspection and maintenance of large scale orbital facilities. In Proceedings of the 2001 ICRA, IEEE International Conference on Robotics and Automation (Cat. No.01CH37164), Seoul, Republic of Korea, 21–26 May 2001; pp. 4180–4185. [[CrossRef](#)]
15. Hu, Q.; Zhang, Y.; Zhang, J.; Hu, H. Formation control of multi-robots for on-orbit assembly of large solar sails. *Acta Astronaut.* **2016**, *123*, 446–454. [[CrossRef](#)]
16. Yang, S.J.; Wen, H.; Jin, D.P. Trajectory planning of dual-arm space robots for target capturing and base manoeuvring. *Acta Astronaut.* **2019**, *164*, 142–151. [[CrossRef](#)]
17. Dong, G.; Zhu, Z.H. Position-based visual servo control of autonomous robotic manipulators. *Acta Astronaut.* **2015**, *115*, 291–302. [[CrossRef](#)]
18. Huang, P.F.; Xu, Y.; Liang, B. Dynamic balance control of multi-arm free-floating space robots. *Int. J. Adv. Robot. Syst.* **2005**, *2*, 117–124. [[CrossRef](#)]
19. Senda, K.; Murotsu, Y.; Mitsuya, A.; Adachi, H.; Ito, S.; Shitakubo, J.; Matsumoto, T. Hardware experiments of a truss assembly by an autonomous space learning robot. *J. Spacecr. Rockets* **2002**, *39*, 267–273. [[CrossRef](#)]
20. Dubowsky, S.; Boning, P. Coordinated control of space robot teams for the on-orbit construction of large flexible space structures. *Adv. Robot.* **2010**, *24*, 303–323. [[CrossRef](#)]
21. Karumanchi, S.; Edelberg, K.; Nash, J.; Bergh, C.; Smith, R.; Emanuel, B.; Carlton, J.; Koehler, J.; Kim, J.; Mukherjee, R.; et al. Payload-centric autonomy for in-space robotic assembly of modular space structures. *J. Field Robot.* **2018**, *35*, 1005–1021. [[CrossRef](#)]
22. Lu, Y.; Huang, Z.; Zhang, W.; Wen, H.; Jin, D. Experimental investigation on automated assembly of space structure from cooperative modular components. *Acta Astronaut.* **2020**, *171*, 378–387. [[CrossRef](#)]
23. Yu, Z.; Liu, X.; Cai, G. Dynamics modeling and control of a 6-DOF space robot with flexible panels for capturing a free floating target. *Acta Astronaut.* **2016**, *128*, 560–572. [[CrossRef](#)]
24. Gasbarri, P.; Pisculli, A. Dynamic/control interactions between flexible orbiting space-robot during grasping, docking and post-docking manoeuvres. *Acta Astronaut.* **2015**, *110*, 225–238. [[CrossRef](#)]
25. Xu, W.; Meng, D.; Chen, Y.; Qian, H.; Xu, Y. Dynamics modeling and analysis of a flexible-base space robot for capturing large flexible spacecraft. *Multibody Syst. Dyn.* **2014**, *32*, 357–401. [[CrossRef](#)]
26. Meng, D.; Liu, H.; Li, Y.; Xu, W.; Liang, B. Vibration suppression of a large flexible spacecraft for on-orbit operation. *Sci. China Inform. Sci.* **2017**, *60*, 050203. [[CrossRef](#)]
27. Meng, D.; Lu, W.; Xu, W.; She, Y.; Wang, X.; Liang, B.; Yuan, B. Vibration suppression control of free-floating space robots with flexible appendages for autonomous target capturing. *Acta Astronaut.* **2018**, *151*, 904–918. [[CrossRef](#)]
28. Grant, M.; Sp, B. CVX: Matlab Software for Disciplined Convex Programming, Version 2.0 Beta. Available online: <http://cvx.com/cvx> (accessed on 5 September 2013).